



The Influence of the Head Model Conductor on the Source Localization of Auditory Evoked Potentials

Stefania Conte¹ · John E. Richards¹

Received: 16 December 2020 / Accepted: 12 September 2021

© The Author(s), under exclusive licence to Springer Science+Business Media, LLC, part of Springer Nature 2021

Abstract

The accuracy of EEG source analysis reconstruction improves when a realistic head volume conductor is modeled. In this study we investigated how the progressively more complex head representations influence the spatial localization of auditory-evoked potentials (AEPs). Fourteen young-adult participants with normal hearing performed the AEP task. Individualized head models were obtained from structural MRI and diffusion-weighted imaging scans collected in a separate session. AEPs were elicited by 1 k Hz and 4 k Hz tone bursts during a passive-listening tetanizing paradigm. We compared the amplitude of the N1 and P2 components before and after 4 min of tetanic-stimulation with 1 k Hz sounds. Current density reconstruction values of both components were investigated in the primary auditory cortex and adjacent areas. Furthermore, we compared the signal topography and magnitude obtained with 10 different head models on the EEG forward solution. Starting from the simplest model (scalp, skull, brain), we investigated the influence of modeling the CSF, distinguishing between GM and WM conductors, and including anisotropic WM values. We localized the activity of AEPs within the primary auditory cortex, but not in adjacent areas. The inclusion of the CSF compartment had the strongest influence on the source reconstruction, whereas white matter anisotropy led to a smaller improvement. We conclude that individualized realistic head models provide the best solution for the forward solution when modeling the CSF conductor.

Keywords Auditory evoked potentials · Source reconstruction · Head models · CSF · WM anisotropy

Introduction

Source analysis identifies the neural generators of the electrophysiological activity recorded on the scalp. A critical aspect of this procedure is the selection of the head model for the forward model and inverse solution. The head model describes both conductivity and geometrical properties of the volume within which the inverse solution is calculated. Thus, it is essential for an accurate source reconstruction that the head model is a realistic representation of the electrical properties of the head. Several studies using simulations have compared the effect of different head models on the source reconstruction. The current data uses source localization of acoustic evoked-potentials (AEP) during an auditory

tetanzation task recorded in young adult participants to compare source reconstruction for different head models.

There are three general types of head models: concentric spheres, boundary element meshes—BEM—and finite element meshes—FEM (for a review on the head model in source analysis, see Hallez et al. 2007; Vatta et al. 2010). The simplest and historically first head model was the spherical model. This model represents the head as a sphere, often with multi-shell nested concentric spheres representing different head media. Each compartment represents one head media type (e.g., scalp, skull, CSF brain) and isotropic conductivity values are assigned throughout each compartment. The spherical model has a semi-analytic forward solution which can be computed with matrix operations (Hallez et al. 2007; Michel and Brunet 2019; Michel et al. 2009; Michel and Murray 2012; Michel et al. 2004). The BEM and FEM models use a realistic geometry of the head derived from structural MRIs (Hallez et al. 2007; Michel et al. 2004). The use of a realistic geometry of the head is important to achieve high accuracy in source localization and it is especially critical for sources placed in the temporal and occipital

Handling Editor: Leon Deouell.

✉ Stefania Conte
contes@mailbox.sc.edu

¹ Department of Psychology, University of South Carolina, Columbia, USA

cortices (Vatta et al. 2010). The BEM models like the spherical models are a compartment model with isotropic conductivity values for each compartment. However, the compartments have a realistic shape corresponding to the shape of a structure in the MRI. Calculations for the BEM model require numerical analysis optimization procedures and thus are more complicated than the spherical models (Hallez et al. 2007). A constraint of the BEM numerical methods is that the conductivities are assumed to be homogeneous throughout each compartment, thus modeled as having isotropic conductivity values. The FEM model characterizes each voxel in the head with a media type and a complex realistic mesh model describes the composition of the head (Hallez et al. 2007; Michel et al. 2004). The FEM mesh model has several advantages over the other model types. The mesh elements can model non-nested media, such as the CSF, which are separate compartments but not nested into one other (e.g., eyes, neck muscle), and provides superior methods to describe complex shapes and boundaries along adjacent material types. The assignment of media conductivity is unconstrained by the numerical estimation method so that anisotropic varying conductivities for a media type may be used.

Conductivity anisotropy has been a topic of concern for head models in source analysis (Bangera et al. 2010; Cho et al. 2015; Güllmar et al. 2010; Hallez et al. 2009; Hau-eisen et al. 2002; Vorwerk et al. 2014; Wolters et al. 2006). Wolters and colleagues (Wolters et al. 2006) measured the effect of anisotropy of skull and white matter (WM) conductivity on the inverse reconstruction of simulated EEG data. They found that WM anisotropy caused the currents to flow in directions parallel to the fiber tracts, whereas the skull anisotropy smeared out the reconstructed signal. Moreover, the effect of the anisotropic conductivity was larger for deep sources surrounded by anisotropic tissues. Similarly, the anisotropic conductivity of the WM influences the accuracy of source localization of EEG data more than MEG data when high-resolution FEM models are utilized. The average localization error of the EEG signal increases especially for deep sources if the WM anisotropy is neglected in the model (Güllmar et al. 2010).

One study examined the effect on the accuracy of source reconstruction of the inclusion of GM, WM, CSF, and anisotropic conductivity for skull and WM (Vorwerk et al. 2014). That study reported in a FEM model that the inclusion of a GM/WM distinction in the brain, and similarly the inclusion of cerebrospinal fluid (CSF) improved the accuracy of source analysis both for location and magnitude effects. The inclusion of the WM anisotropy had significant effects on the quality of source localization, although of a smaller magnitude compared to the CSF and GM/WM distinction in the brain (Vorwerk et al. 2014).

Most of the studies of the role of head model construction have used simulation procedures where an artificial current source is placed inside the head and the forward model/inverse source reconstruction is used to compare the topography and amplitude of the computed source reconstruction with the simulated current source. The current study used data from an auditory evoked potential (AEP) task and examined the effect of different head models on the source reconstruction for the experimental data (Bangera et al. 2010; Birot et al. 2014; Lee et al. 2009). A group of healthy adult participants took part in an EEG recording session with auditory stimuli resulting in “tetanization” of the AEP. The tetanization procedure involves the rapid and repeated presentation of single auditory tone, preceded and followed by a two-tone AEP presentation to assess pre-post differences in the AEPs. The sensory tetanization is hypothesized to result in long-term potentiation (LTP) effects in the auditory cortex. The potentiation effects are specific to only the auditory N1 component, or with visual stimuli, the visual N1B component (see review by Sanders et al. 2018). If the tetanization effects found in the AEP N1 component are generated in a specific auditory cortex area, then source reconstruction of the N1 component would reveal the site of the LTP. In the current paper we use these experimental data to test the effects of a range of head models on the source reconstruction, to extend evidence of simulation studies to datasets collected in an experimental setting. The source reconstruction should provide important information about the neural generator(s) of LTP-like effects.

There were two goals of the current study. First, we assessed the AEPs (i.e., N1 and P2 components) in response to auditory stimuli before and after tetanic stimulation in young adult participants. We used distributed source analysis to assess the cortical sources of the AEP in response to un-tetanized and tetanized stimuli. We created individualized head models by collecting structural MRI volumes for all participants. We predicted that only the AEPs in response to the tetanized stimulus would be enhanced. The potentiation effect would be localized in the auditory cortex contralateral to the stimulation and result in larger current density reconstruction (CDR) values for the tetanized stimulus vs. the un-tetanized stimulus. Second, we compared the source reconstruction of the AEPs with a series of head models based on different segmenting methods, models that did or did not include CSF, and models with conductive anisotropy in the WM segments. WM anisotropy was quantified by using information from the DTI acquisitions, including fractional anisotropy (FA) and diffusion tensors. We expect that the source reconstruction of the effects would be most accurate with the head models that realistically modeled the entire head rather than compartment models or models with limited media elements.

Methods

Subjects

Fourteen volunteers (mean age: 23 years; SD 4 years; 5 male) recruited from the University of South Carolina participated in this study. All participants were right-handed and reported normal hearing and no history of neurological impairments. Participants were compensated for their time and gave written informed consent as approved by the Institutional Review Board at University of South Carolina.

Stimuli and Procedure

Participants were presented with sounds through earphones while the EEG was recorded. Tone bursts of 1 kHz and 4 kHz were digitally created using Audacity software (version 2.3.0) and saved as WAV files. Participants wore Etymotic Research headphones plugged into the E-Prime SR Box. Sounds were played monaurally to the right ear, while the left headphone was kept in place but muted to reduce the level of environmental noise. All participants were run in an ABA design (see Fig. 1). Sounds were of 50 ms in duration with interstimulus intervals between 1800 to 2200 ms and were presented during the pre- and post-tetanzing phases (A). Trains of 1 kHz stimuli were presented at a high frequency rate (i.e., 13 Hz) during the tetanizing phase (B). Twenty-four trains, 10 s each, were presented during the 4 min of tetanization. A 10-min break separated the tetanizing phase from the post-tetanzing recording. Participants sat in an electrically shielded and sound-attenuated room and passively listened to the sounds while reading quietly. We collected the location of the HGSN electrodes with a geodesic photogrammetry system (GPS) dome (Russell et al. 2005) at the end of each EEG task. In a separate session we collected structural

MRI and diffusion-weighted imaging (DWI) from each participant.

EEG Recording and Data Analysis

Continuous EEG recordings were carried out using a high-density Electrical Geodesics Inc. (Philips-Neuro, Inc; EGI, Inc; Tucker, 1993; Tucker et al. 1994) 128-channel Ag/AgCl electrode nets (HydroGel Geodesic Sensor Net, HGSN). The EEG was acquired by Net Station (version 3.0) with 20 K amplification. The signal was recorded at a 250 Hz sampling rate and band-pass filtered 0.1 Hz to 100 Hz. Impedances were kept below 100 k Ω . The EEG signal was referenced to vertex during the recording.

EEG processing, artifact detection and rejection, and ERP averaging were carried out using the EEGLAB (Version 14.1.2; A. Delorme and Makeig 2004) and ERPLAB (Version 7.0.0; Lopez-Calderon and Luck 2014) MATLAB toolboxes. Details of the EEG preprocessing procedure can be found in Gao et al. (Gao et al. 2019). The PREP pipeline MATLAB toolbox (Bigdely-Shamlo et al. 2015) was used to perform a robust re-referencing of the signal. A band-pass 8th order Butterworth filter of 0.1–42 Hz was applied to the EEG signal and then the EEG was segmented into epochs surrounding the onset of the sounds (– 100 ms to 1000 ms) and baseline corrected relative to 100-ms baseline period. An automatic artifact detection was applied to exclude trials with excessive activity. A threshold of ± 200 μ V was applied on the first 500 ms after stimulus onset, while a threshold of ± 400 μ V was applied between 500 and 1000 ms. Extended independent component analysis (ICA; Delorme and Makeig 2004; Delorme et al. 2007; Jung et al. 2000) was utilized to identify and remove eye-movement and eye-blink components. The remaining trials were visually inspected to detect motor movements or other artifacts. Channels with artifact were substituted with artifact-free channels using a spherical spline interpolation routine (Delorme and Makeig 2004). Trials with more than 12 bad channels were not considered for further analysis. On

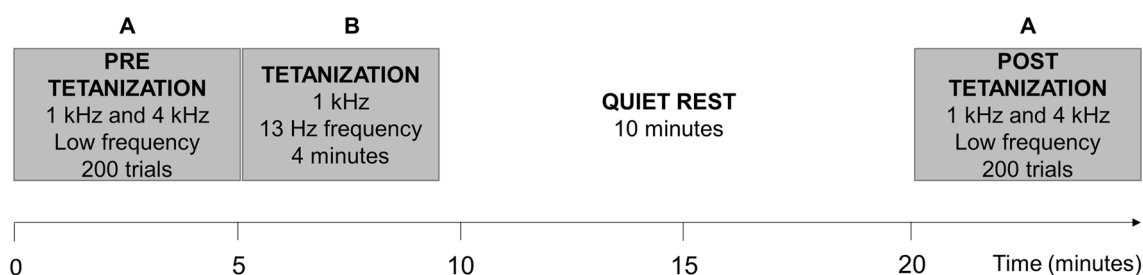


Fig. 1 Schematic representation of the experimental procedure during the EEG recording. Both 1 kHz and 4 kHz tone bursts were randomly presented at a low frequency during pre- and post-tetanzing phases (A). The tetanization phase (B) consisted in the presentation of 1 kHz

sounds at high frequency (13 Hz) for 4 min. This stimulation was followed by ~ 10 min of quiet rest. All participants were quietly reading while listening at the presented stimuli

average we removed < 15% of trials per condition (Pre1kHz: $M = 11.93\%$; Pre4kHz: $M = 12.92\%$; Post1kHz: $M = 13.82\%$; Post4kHz: $M = 13.34\%$). Group average waveforms were computed for both sound types (i.e., 1 kHz and 4 kHz) and phases (pre- and post-tetanzing phase).

Peak-to-trough differences were calculated for the N1 and P2 AEPs by subtracting the amplitude of the preceding peak to the amplitude of the component of interest. Amplitude of 10 ms surrounding the peak of each AEP component were extracted for the entire 128 HGSN channels for source analysis. Electrode locations were transformed into the 10–10 system for AEP analyses by applying a spherical spline interpolation of the 128-channel data (Richards et al. 2018). Only fronto-central electrodes (F3, F1, Fz, F2, F4; FC3, FC1, FCz, FC2, FC4; C3, C1, Cz, C2, C4) were analyzed for AEP analyses.

MRI and DTI Data Acquisitions

The MRI and DWI volumes were acquired during one session on a Siemens Magnetom Prisma 3.0 T scanner (Siemens, Erlangen, Germany) with a 20-channel head-coil. Whole-head T1-weighted images were acquired using an MP-RAGE protocol. The T1 scan included the following parameters: repetition time (TR) = 2250 ms, echo time (TE) = 3.65 ms, flip angle (FA) = 9° , field of view (FoV) = 256×256 pixels, voxel size = $1.0 \times 1.0 \times 1.0$ mm. The total acquisition time was of 6 min and 17 s. T2-weighted images were acquired using an SPC sequence lasting for 5 min. The following parameters were considered: TR = 3200 ms, TE = 567 ms, FoV = 256×256 pixels, voxel size = $1.0 \times 1.0 \times 1.0$ mm.

The DWI data were acquired with the following parameters: TR = 4500 ms, TE = 103 ms, FA = 90° , FoV = 220×220 pixels, 58 slices, and voxel size of $2.2 \times 2.2 \times 2.2$ mm. Monopolar diffusion weighting was performed along 137 independent directions, with a b-value of 2000 s/mm^2 . We acquired two DWI sequences with opposite phase encoding directions (anterior–posterior and posterior–anterior), each one lasting 10 min and 35 s, and a single-band reference (SBref) image (e.g., Human Connectome Project, https://www.humanconnectome.org/storage/app/media/documentation/data_release/October2012_Release_User_Guide.pdf). Each DWI sequence included ten images without diffusion-weighting (i.e., $b = 0$) with distortions going in opposite directions. These b0 scans were used for distortion corrections.

Image Processing and ROI Definition

The MRI volumes were used to obtain realistic head models of all participants for source analysis. The T1 MRI volume was segmented into an outer scalp compartment and a skull

compartment inside the scalp compartment. The inner part of the skull compartment, the “brain”, was differentiated into GM, WM, T2W-defined CSF, and dura. Additional segmenting was conducted to differentiate the eyes, muscle, and nasal cavity. Details about the segmenting procedure can be found in the Supplementary Material S1 and elsewhere (Gao et al. 2019; Richards, 2013). Tissue segmentation results are depicted in Fig. 2. Tetrahedral parcellation was utilized to create meshes of each segmented compartment (average node number = 31,565). Conductivity values of each segment were as follow: scalp 0.35 S/m, skull 0.0132 S/m, CSF 1.79 S/m, WM 0.2 S/m, GM 0.33 S/m, dura 0.33 S/m, muscles 0.35 S/m, eyes 0.5 S/m, and nasal cavity 0.0048 S/m.

The DTI volumes were used to create anisotropic conductivity for the WM materials. Diffusion-weighted data were processed using the tools implemented in FSL (version 6.0.1; www.fmrib.ox.ac.uk/fsl). First, the geometrical distortion of the DTI volumes was estimated using two b0 images with opposing polarities of the phase-encode blips. The susceptibility-induced off-resonance field was estimated using a method similar to that described in Andersson et al. (2003). FSL’s TOPUP (Andersson et al. 2003; Smith et al. 2004) was used to obtain distortion corrected images. Data were corrected for current-induced distortions and motion artifacts using Eddy correction tool (Andersson and Sotiropoulos 2016) and then registered to the whole head MRI volume with the FSL `epi_reg` tool.

A method to compute anisotropic conductivity is based on the assumption that the conductivity tensor in WM is linearly proportional to the diffusion tensor found in DTI (Basser et al. 1994; Tuch et al. 2001). This method has been used to estimate WM anisotropic conductivity in several studies (Güllmar et al. 2010; Haueisen et al. 2002; Johannes Vorwerk et al. 2014). We calculated anisotropic conductivity values of the white matter (WM) from the DTI using three different approaches, i.e., longitudinal (axial) diffusivity (LD, i.e., λ_1), fractional anisotropy (FA), and conductivity tensor (DTI). For the LD and FA anisotropic conductivity values, the conductivity of a WM voxel was the WM conductivity value (see values listed in the previous paragraph) multiplied by the voxel’s corresponding LD or FA value. A scaling factor was applied to the LD and FA models so that the sum of the anisotropic voxels was approximately equal to the sum of the WM voxels in the isotropic WM models. For the DTI anisotropic conductivity values, the diffusion tensor for each voxel was used to modify the 3-D matrix of anisotropic directions for the voxel (Cho et al. 2015; Vorwerk et al. 2014). A scaling factor was applied to the conductivity tensor to preserve the sum of the anisotropic voxels being approximately equal to the sum of the WM voxels in the isotropic WM models. Eigenvalues of the conductivity tensor were normalized by the corresponding isotropic

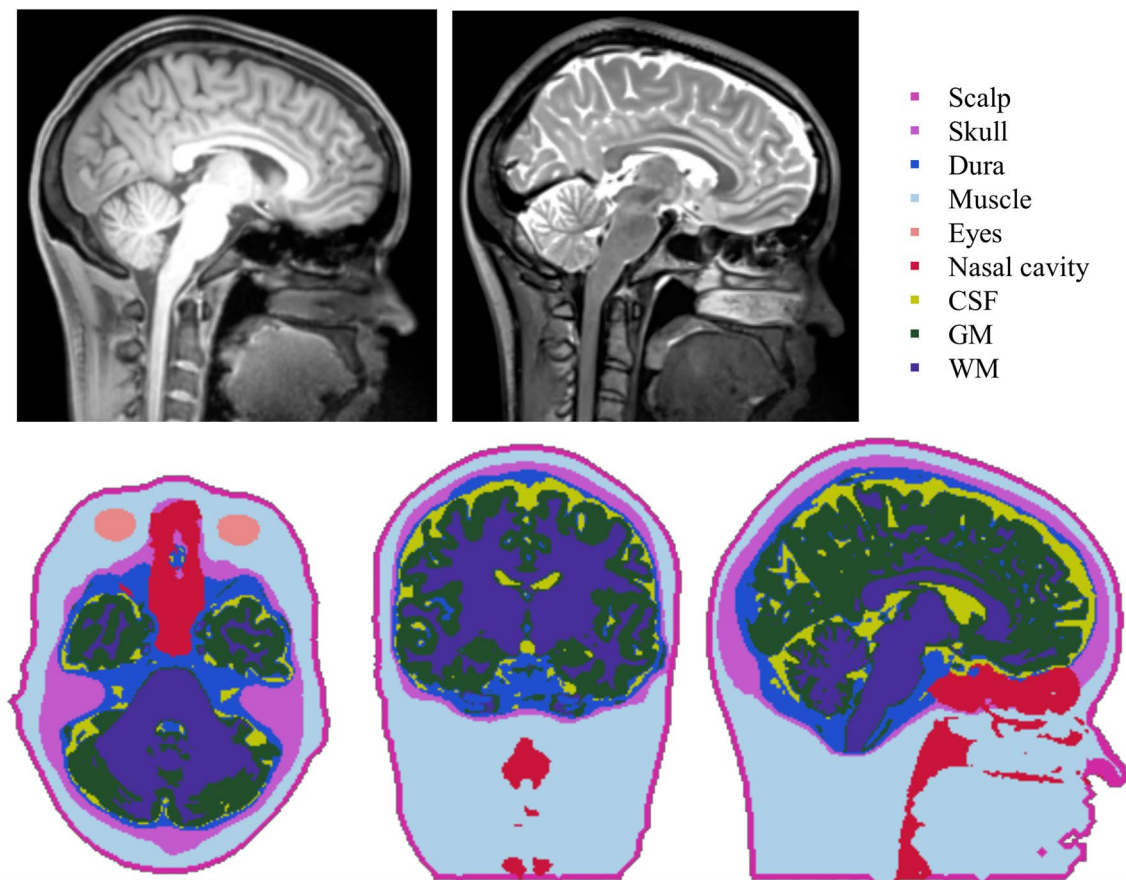


Fig. 2 Sagittal view of T1-weighted and T2-weighted volumes for a representative participant (top). Multiplanar view of the head volume conductor of a representative participant. The different head compart-

ments of the most complex head model included in our study (i.e., 9-FEMmesh *Standard*) are depicted with different colors (bottom)

tensor in a way that kept unchanged both anisotropy ratio and eigenvectors of the tensors (Cho et al. 2015; Vorwerk et al. 2014).

Anatomical regions of interest (ROIs) were defined based on stereotaxic atlases for each individual participant MRI. Jülich (Eickhoff et al. 2007) and the LONI Probabilistic Brain Atlas (LPBA; Shattuck et al. 2008) brain atlases were utilized to define 25 anatomical areas. We selected three areas within the primary auditory cortex (A1) from the Jülich atlas (i.e., TE1.0, A1 core; TE1.1, A1 caudal; TE1.2, A1 rostral. Morosan et al. 2001) and three adjacent areas within the temporal lobe (i.e., superior temporal gyrus, STG; middle temporal gyrus, MTG; posterior inferior temporal gyrus, pITG). The Jülich atlas was calculated for each participant MRI by registering/transforming the Jülich atlas to an age-appropriate template (i.e., 20–24 Years; Richards et al. 2015; Richards and Xie 2015) and then into the MRI of each participant (Gao et al. 2019). The LPBA atlas was created for each subject from the 40 segmented adult heads of the LONI atlas database (Shattuck et al. 2008), each registered/transformed into the individual MRI, and ROIs assigned to

voxels for individuals with a majority vote procedure (Fillmore et al. 2015).

ERP Source Analysis

The source analysis used realistic head models current density reconstruction with the Fieldtrip toolbox, and a variety of head models (Buzzell et al. 2017; Richards, 2013; Richards et al. 2018). Realistic head models were derived from individual MRIs. Source analysis was conducted applying the CDR technique and the finite element method (FEM) to solve the forward problem using the Fieldtrip toolbox (Oostenveld et al. 2011) and SimBio method (Vorwerk et al. 2013; Vorwerk et al. 2018). The forward model was calculated from the segmented head model (see Table 1). The source location was constrained to the grey matter segmented from each participant's MRI with a 3-mm grid. Electrode locations were defined based on the GPS acquisition and co-registered to the head mask derived from the MRI of each participant. The lead-field matrix was defined based on the source location, electrode

Table 1 List of models with their respective media types

Model name	Method	Scalp	Skull	Brain	CSF	GM	WM	Other
Concentric spheres	direct	x	x	x	x	—	—	—
BEM dipoli	BEM	x	x	x	x	—	—	—
3-compartment	FEM	x	x	x	—	—	—	—
4-FEMmesh CSF	FEM	x	x	x	x	—	—	—
4-FEMmesh WM	FEM	x	x	*	—	x	x	—
4-FEMmesh LD	FEM	x	x	*	—	x	x ^a	—
4-FEMmesh FA	FEM	x	x	*	—	x	x ^a	—
4-FEMmesh DTI	FEM	x	x	*	—	x	x ^a	—
5-FEMmesh WM	FEM	x	x	*	x	x	x	—
5-FEMmesh LD	FEM	x	x	*	x	x	x ^a	—
5-FEMmesh FA	FEM	x	x	*	x	x	x ^a	—
5-FEMmesh DTI	FEM	x	x	*	x	x	x ^a	—
9-FEMmesh <i>Standard</i>	FEM	x	x	*	x	x	x	x
9-FEMmesh <i>Standard</i> LD	FEM	x	x	*	x	x	x ^a	x
9-FEMmesh <i>Standard</i> FA	FEM	x	x	*	x	x	x ^a	x
9-FEMmesh <i>Standard</i> DTI	FEM	x	x	*	x	x	x ^a	x

The first three models were “compartment” models with nested compartments representing the head media. The 4-FEM mesh and more complex models were represented by voxel-wise element identification of head media. The media that were included are marked with “x”; the media that were not included are marked with “—”. “x^a” indicates that anisotropic conductivity values were considered for the included media. “x” in the brain column indicates the brain compartment was not distinguished into GM and WM, “*” in the brain column indicates WM and GM were distinguished in the brain. “Other” media types were dura, muscle, eyes, and nasal cavity

location, forward model, and conductivity values for each material. The Concentric Sphere model used semi-analytic methods for the forward model and lead-field matrix. The BEM dipoli model (Oostendorp and van Oosterom 1989) used BEM to estimate the forward solution and lead-field matrix. The FEM mesh models used the SimBio (Vorwerk et al. 2013; Vorwerk et al. 2018) method to estimate the forward model and lead field matrix along with the eLORETA method (Pascual-Marqui, 2007; Pascual-Marqui et al. 2011; Pascual-Marqui et al. 2006) for estimating the current density values. The time for the source analysis was centered on the individually identified peak of the AEP component.

There are some advantages to using an equivalent current dipole approach that localize well-defined sources. However, in experimental situations with complex human activities, sources are often due to non-experimental effects and are spread throughout the head. Thus, we adopted a distributed approach that assumes as sources all possible location simultaneously. Therefore, any distribution of activity would produce a resolution estimate. We utilized the eLORETA method to the inverse solution given its advantages with experimental data compared to other similar distributed methods (e.g., sLORETA; Jatoi et al. 2014). The use of eLORETA has been validated for the localization of neural activity in primary and secondary sensory cortices in experimental settings (Pascual-Marqui et al. 2011).

Head Model Definition

The source analysis was done using head models of varying complexity and assumptions (Table 1). The concentric spheres model was a compartment model with isotropic values for scalp, skull, CSF, and brain. Note that CSF is modeled as a compartment surrounding the brain, so that the CSF in ventricles in the inner compartment was not represented. The boundary element method (BEM) model used isotropic values for the same four media types, with realistic shapes for the four compartments. The 3-FEM model used isotropic values of the scalp, skull, and brain (i.e., 3-compartment model) in a FEM mesh via the SimBio procedure. The subsequent FEM models were extensions of this model which included CSF, differentiation of the brain into WM and GM, and anisotropic conductivity values for WM. One 4-FEM model included CSF as a media type in the mesh inside the brain compartment, distinguishing brain and CSF. Another 4-FEM model distinguished GM and WM in the brain compartment. Three further 4-FEM models were developed from GM-WM head model by introducing anisotropic WM values in the model, namely LD, FA, and DTI (see *Image processing and ROI definition*). The 5-FEM mesh model included CSF, GM and WM distinctions in the brain compartment, and the three variants of WM anisotropy calculation (i.e., 5-FEM mesh LD/FA/DTI). Finally, the most realistic head model included a total of nine media types,

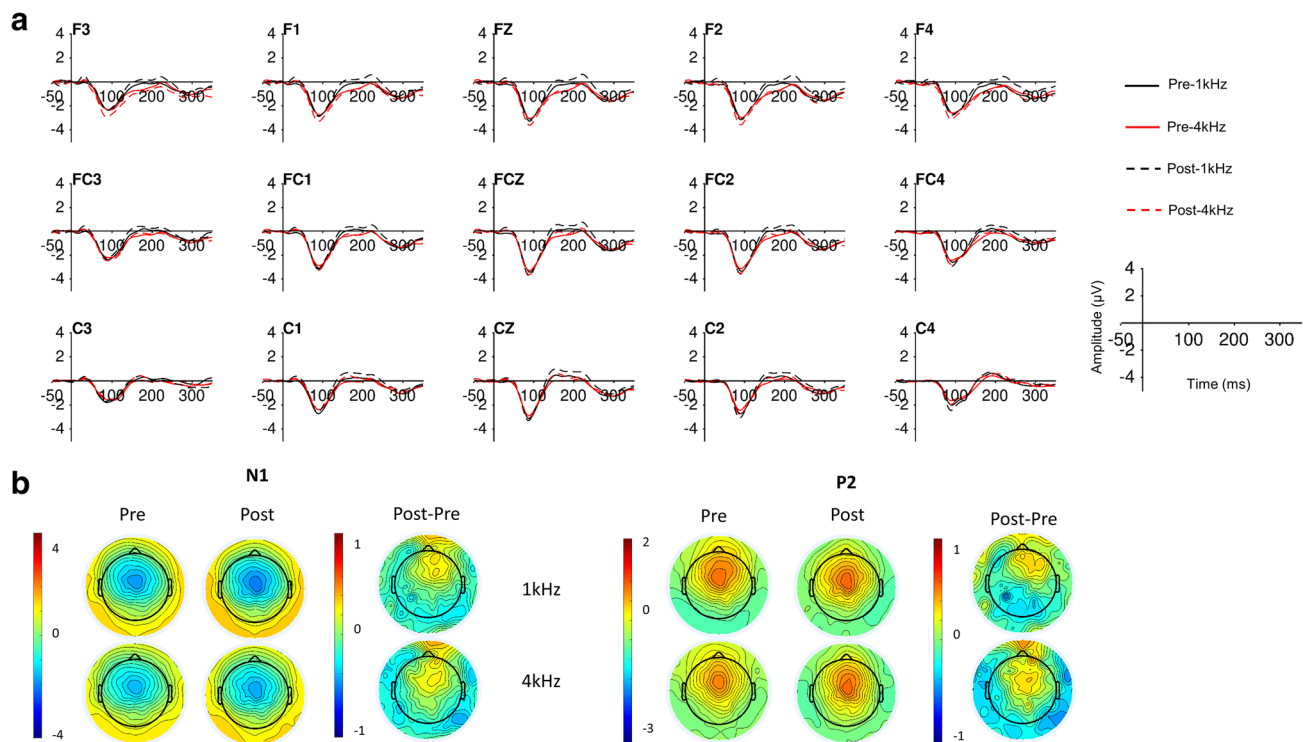


Fig. 3 Top panels: line graphs of the grand average ERP response as a function of Stimulus and Phase over frontal and central electrodes. Bottom panels: topographical map of the ERP response at the peak

of N1 (right) and P2 (left) components as a function of Phase, along with the differential activity obtained subtracting the pre- to the post-tetanizing ERP response

i.e., an outer scalp compartment; a skull compartment; CSF, GM, WM, and dura inside the skull compartment; eyes, muscle, and nasal cavity inside the scalp compartment but outside the skull compartment (Richards, 2013), with and without modeling of WM anisotropy. We named this model the 9-FEM *Standard* because it has been the standard procedure utilized in previous studies of our lab (Buzzell et al. 2017; Conte et al. 2020; Gao et al. 2019; Richards, 2013).

Results

The analytic strategy began with the examination of the LTP-like effect on the N1 and P2 AEPs and their neural generators reconstructed with the head model approach previously implemented in our lab (i.e., 9-FEMmesh *Standard*). Results of these analyses are reported in the *ERP results* and *Source analysis results* paragraphs, respectively. Then, we directly compared the modulation of our experimental factors and the solution obtained with a range of head models. We further compared the different models using a correlational approach and calculating the relative topography change with complex models as references. Results of these analyses are reported in the section entitled “*Model comparison*”. We performed direct comparisons between isotropic

and anisotropic solutions on both N1 and P2 sources (“*Isotropic and Anisotropic Model Comparison*” section). Finally, we utilized the CDR values in auditory areas to simulate the EEG activity on the scalp. The model comparisons of simulated solutions were conducted using RDM and InMAG values with complex models as references. Results are reported in the section “*Simulated EEG from source*”.

ERP Results

Peak-to-through values were examined as a function of Sound (1 kHz vs. 4 kHz) and Phase (pre vs. post) over fronto-central channels. Figure 3a depicts the ERP grand average responses for the four experimental conditions across electrodes. Both the N1 and P2 show a clear peak in all the considered fronto-central electrodes. The scalp distribution of the AEP activity at the peak of both N1 and P2 components is represented in the topographical maps of Fig. 3b as a function of Sound and Phase. Increased activity of both AEP components is evident during the post-tetanizing phase. In the subtraction maps (“Post–Pre”) the AEP activity during the pre-tetanizing phase has been subtracted to the activity at the peak of the component during the post-tetanizing phase.

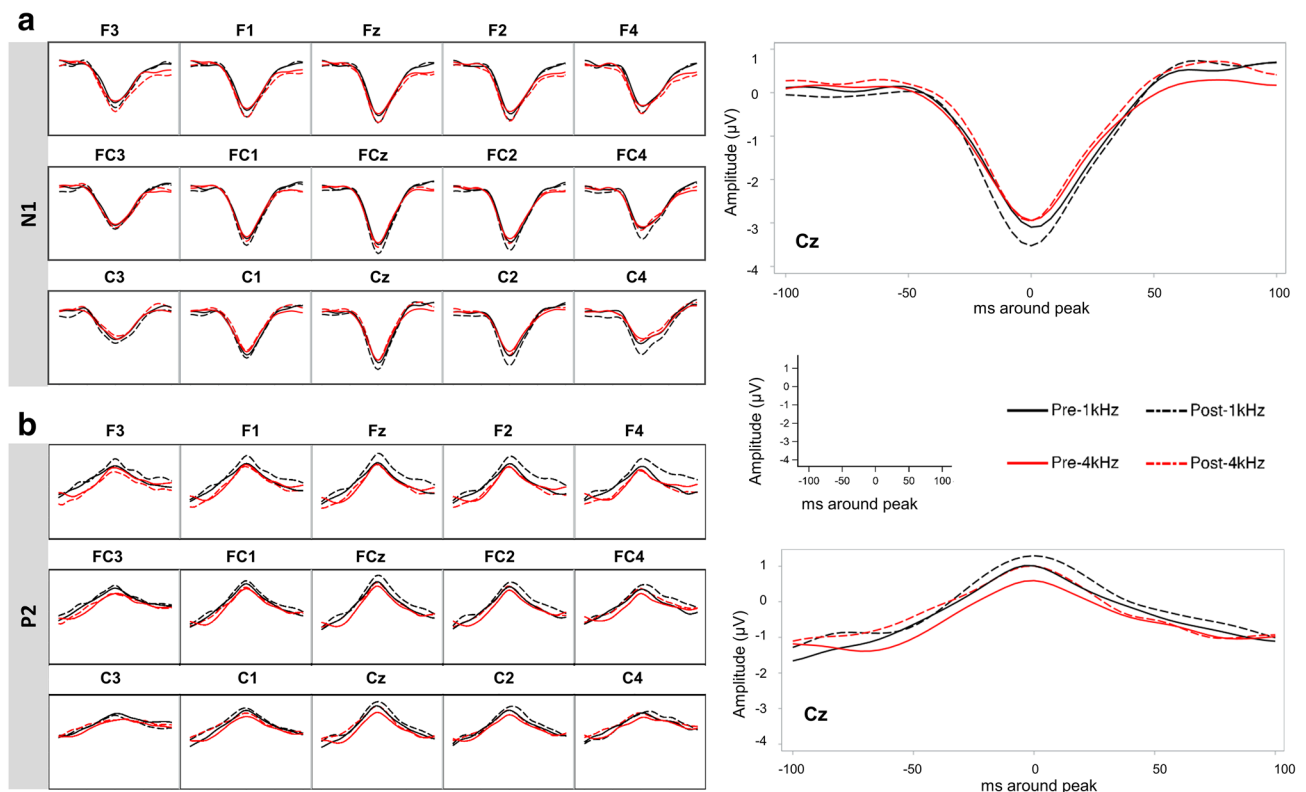


Fig. 4 ERP response at the N1 (top) and P2 (bottom) peak as a function of Sound and Phase over frontal and central electrodes. The P2 response showed an increase in amplitude after the tetanizing phase. The tetanizing effect is mainly visible for the 1 kHz sound

A multivariate GLM approach to repeated measures was utilized to analyze the groups of electrodes and experimental factors as multiple dependent variables. Amplitude values at the peak of both N1 and P2 AEP components were analyzed using the Proc GLM of SAS (version 9.4) software (SAS Institute Inc., Cary, NC) as a function of Sound, Phase, and Electrode location.

We found for the N1 amplitude main effects of Electrode location [$F(14, 182) = 8.49, p < 0.0001$] and Phase ($1, 13 = 13.92, p = 0.0025$). There were significant interactions between Sound and Electrode [$F(14, 182) = 3.79, p < 0.0001$] and between Sound, Phase, and Electrode [$F(14, 182) = 1.93, p = 0.0259$]. Univariate tests for the individual electrodes showed that a large variance of the interaction between Stimulus and Phase was explained by central and fronto-central channels, i.e., C2 ($\eta^2 = 0.124$), FC4 ($\eta^2 = 0.134$), Cz ($\eta^2 = 0.120$), C4 ($\eta^2 = 0.276$), and C3 ($\eta^2 = 0.386$). Follow up comparisons in these channels showed a significant increase in N1 amplitude after the tetanizing phase for the 1 kHz ($p < 0.0001$), but not 4 kHz ($p = 0.6204$) sound. Amplitudes surrounding the peak of the N1 at each fronto-central channel are displayed in Fig. 4a.

The tetanizing effect was investigated around the peak amplitude of the P2 AEP over fronto-central channels. Results showed only a significant main effect of Electrode

location [$F(14, 182) = 3.28, p < 0.0001$]. Figure 4b represent the ERP pattern for the experimental conditions around the peak of the P2 component over fronto-central electrodes.

Source Analysis Results

The cortical sources of both N1 and P2 ERP components were investigated considering the head model and forward method utilized in previous studies from our lab, namely the 9-FEMmesh *Standard* model. Current density values were analyzed as a function of Sound (1 kHz vs. 4 kHz), Phase (pre vs. post), and Side (left hemisphere vs. right hemisphere) over the areas within the primary auditory cortex (i.e., A1 core, A1 caudal, and A1 rostral) and surrounding areas within the temporal lobe (i.e., STG, MTG, and pITG). Figure 5 displays the anatomical ROIs and the N1 and P2 average CDR for the 1 kHz sound pre- and post-tetanizing phase plotted on a 3D rendering of the average MRI template. An increased activity in the primary auditory cortex was visible after the tetanizing phase for both the N1 and P2 AEP components. There were other areas that were active as the source for these components, such as the central-superior areas shown in Fig. 5b. However, these were not different in the pre- and post-phases (“Post–Pre 1 kHz” in Fig. 5b).

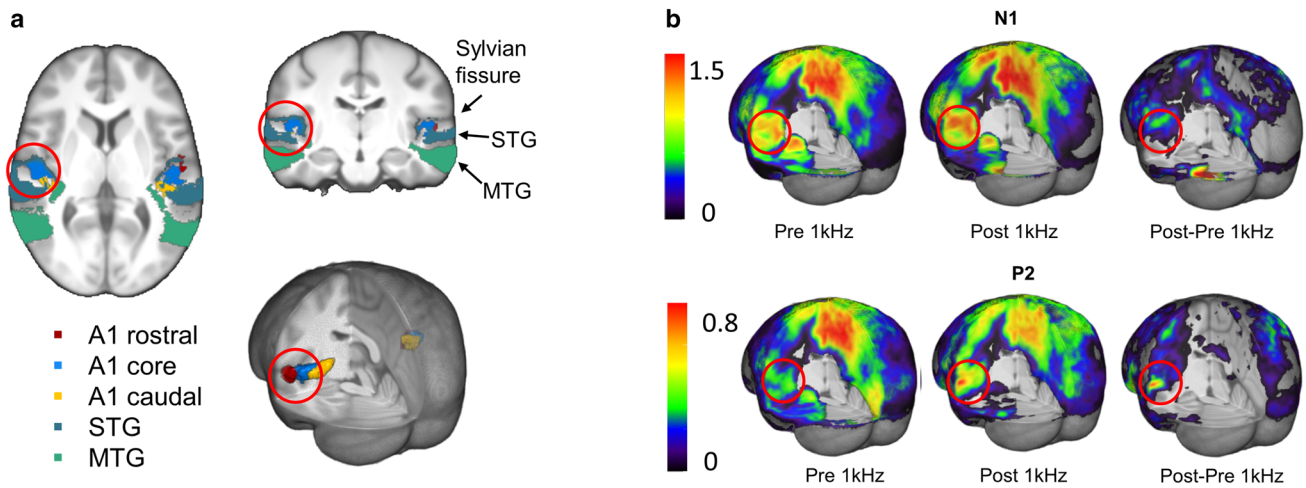


Fig. 5 **A** Axial, coronal, and 3D rendering view of the anatomical ROIs plotted on an average MRI template. In the rendering view we removed left occipital lobe, posterior lobe, and the posterior portion of the temporal lobe to better show the primary auditory areas. **B**

Average CDR values at the peak of N1 and P2 ERP components plotted on an average MRI template as a function of phase. The red circle marks an approximate region around the A1 areas

Our analyses focused on the primary auditory areas and surrounding regions of the temporal lobe.

We investigated the effect of experimental conditions on the N1 source. Results of the N1 source analysis revealed a significant main effect of ROI [$F(5, 65) = 2.48, p = 0.0403$]. The ROI effect was better qualified by a significant interaction between ROI and side [$F(5, 65) = 23.61, p < 0.0001$]. There was a significant Sound by Phase interaction [$F(1, 13) = 4.74, p = 0.048$]. Univariate ANOVAs for each brain region showed a significant side effect over the core and rostral segments of primary auditory areas [$F(1, 13) > 17.46, p < 0.0011$], but not the remaining ROIs [$F(1, 13) < 4.16, p > 0.0622$]. Figure 6a shows the CDR values at the N1 peak as a function of side across the considered ROIs. Larger activity was elicited in the left compared to the right primary auditory areas (i.e., A1 core and rostral segments). Simple effects were further examined through the calculation of the eta-squared values. The variance of the side factor was mainly explained by the A1 rostral area ($\eta^2 = 0.651$).

Univariate ANOVAs for each sound type showed a significant Phase effect for the 1 kHz sound [$F(1, 13) = 5.19, p = 0.0402$], but not for the 4 kHz sound ($F(1, 13) = 0.74, p = 0.4066$). Figure 6b shows the CDR at the N1 peak for all four conditions. Larger CDR values characterized the response to the 1 kHz sound during the post-tetanzing than pre-tetanzing phases.

Sound and Phase main effects were significant for the P2 AEP component, respectively $F(1, 13) = 7.12, p = 0.0193$ and $F(1, 13) = 14.01, p = 0.0025$. The responses to the 1 kHz sound ($M = 4.29; SD = 1.95$) and during the post-tetanzation phase ($M = 4.35; SD = 1.94$) were larger than the 4 kHz

sound ($M = 3.84; SD = 1.83$) and pre-tetanzation phase ($M = 3.76; SD = 1.82$). There was a significant ROI by side interaction [$F(5, 65) = 15.49, p < 0.001$]. The P2 CDR values across ROIs are depicted in Fig. 6 (right panel). Univariate ANOVAs showed significant side effects for the A1 core and rostral brain areas [$F(1, 13) > 12.90, p < 0.0033$] but not for the remaining areas [$F(1, 13) < 3.03, p > 0.1052$]. Simple effects, performed by means of the eta-squared, showed that the largest side variance was explained by the A1 rostral area ($\eta^2 = 0.599$).

Model Comparison

One aim of the study was to investigate whether including WM anisotropy values in the head model exerts an effect on the source reconstruction. We calculated WM anisotropy values using three alternative algorithms, namely LD, FA, and DTI (for details see Image processing and ROI definition section) applied to the 4-FEMmesh, 5-FEMmesh, and 9-FEMmesh *Standard* solutions. Figure 7 depicts an anisotropic distribution of WM conductivity for a representative participant estimated by two of the algorithms used in the current study. The peak of conductivity distribution was at 0.2 S/m for both measures. This value corresponds to the conductivity value utilized for the WM segment in our head models.

First, we wanted to compare the solutions obtained by modeling WM anisotropy with three alternative methods. Figure 8 displays the CDR values surrounding the peak of N1 and P2 AEP components obtained applying the three anisotropy calculations (i.e., DTI, FA, and LD bars).

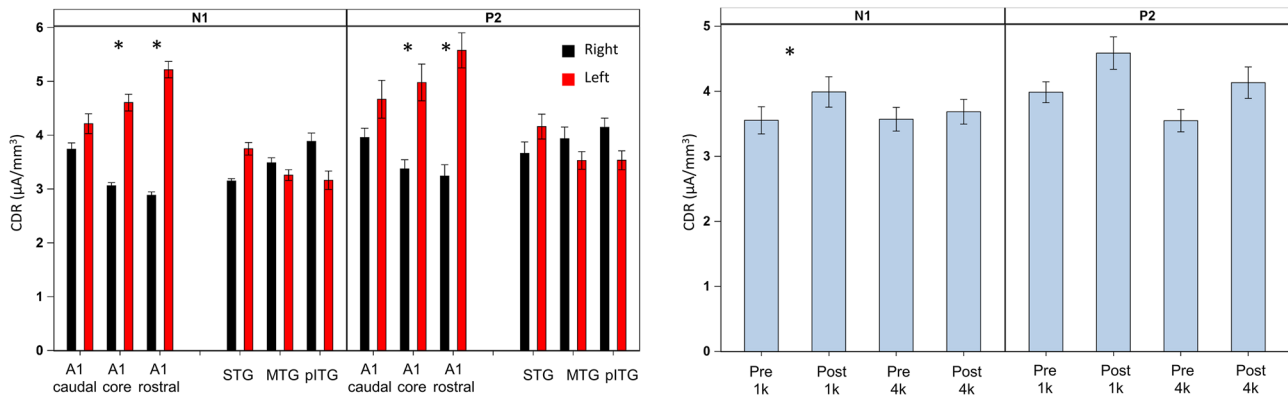


Fig. 6 Bar charts represent the CDR values around the peak of N1 and P2 components as a function of Hemisphere across a series of areas in the primary and secondary auditory cortices (left panels) and Sound (right panels). CDR values are larger over the left than right

hemisphere only in the portions of the Heschl's gyrus (A1 regions). The CDR response to the 1 k Hz sound was larger than the 4 k Hz sound for the N1 component. Significant differences are marked with *

Comparable solutions were obtained for all the considered head models. Univariate ANOVAs showed nonsignificant difference between the solutions for all head models (4-FEMmesh: $F(2, 26) < 1.26$, $p > 0.285$; 5-FEMmesh: $F(2, 26) < 1.10$, $p > 0.333$; 9-FEMmesh *Standard*: $F(2, 26) < 1.17$, $p > 0.311$). For this reason, we included in further

analyses only the most complex calculation of WM anisotropy (i.e., DTI).

We compared the effect of our experimental conditions on the source reconstructed values obtained with progressively more complex head models. Figure 9 displays the 3D rendering of the CDR values around the peak of the N1 (top panels) and P2 (bottom panels) components as a function

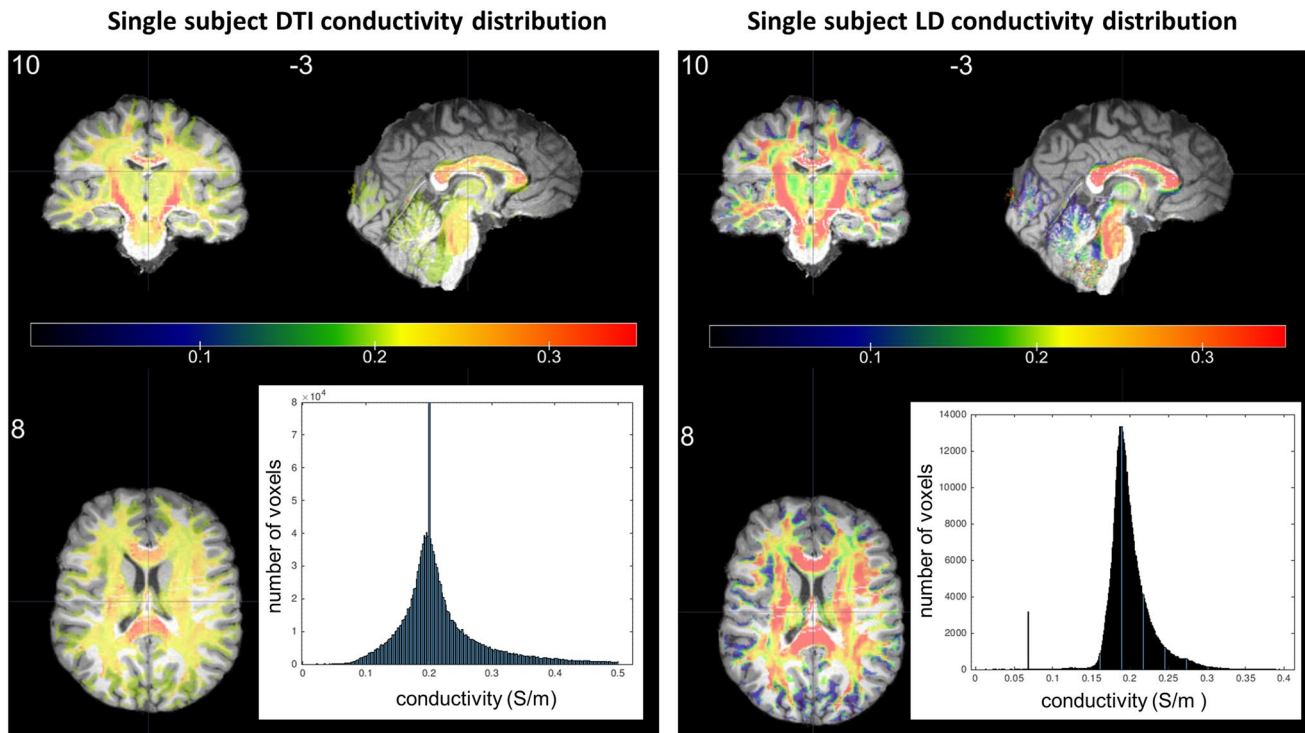


Fig. 7 Multi-planar representation of the distribution of WM conductivity values calculated with the DTI method (left) and LD method (right) plotted on a single participant brain. The histograms represent

the frequency distribution of conductivity values for each method of calculation (i.e., DTI and LD)

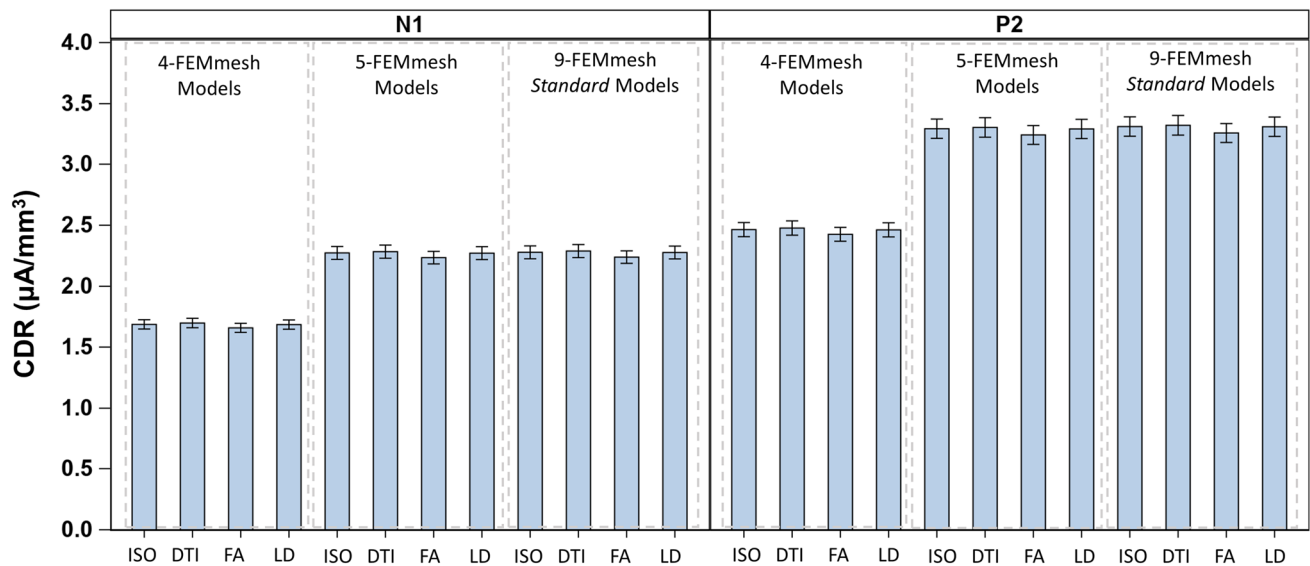


Fig. 8 Bar charts represent the CDR values around the peak of N1 (left) and P2 (right) components across primary and secondary auditory areas. The isotropic solution (ISO) and anisotropic solutions including three alternative WM measures (DTI, FA, and LD) are

depicted for the standard, 4- and 5-FEMmesh models. CDR values within model were similar each other, while lower CDR values were obtained with the 4-FEMmesh models compared to both 5-FEMmesh and 9-FEMmesh *Standard* models

of Phase and head model. Widespread CDR activity for both AEP components resulted from the Concentric Sphere head model. The solution obtained by modeling the CSF (4-FEMmesh CSF) was similar to the solutions that provided more realistic head representations. Comparable CDR distributions were obtained by modeling anisotropic (5-FEMmesh DTI) and isotropic WM values (9-FEMmesh *Standard*). Results of simpler 4-FEMmesh models were more similar to the results of complex models when the CSF, rather than WM anisotropy, was included in the model. Modeling the CSF, but not WM anisotropy, resulted in a more comparable solution to the one obtained with more complex head models. All head models showed an increase in the CDR activity after the tetanizing phase.

We directly compared the source localization obtained with our usual model type (i.e., 9-FEMmesh *Standard* model) and other models created using different methods to solve the forward solution (direct or BEM compared to FEM) and modeling fewer head media. In a multivariate ANOVA the CDR values around the peak of N1 and P2 AEP components were analyzed as a function of Sound (1 kHz vs. 4 kHz), Phase (Pre vs. Post), ROI (A1 core, A1 caudal, A1 rostral, STG, MTG, and pITG), and Model (Concentric Sphere, BEM dipoli, 3-compartment, 4-FEMmesh CSF, 4-FEMmesh DTI, 5-FEMmesh DTI, 9-FEMmesh *Standard*, and 9-FEMmesh *Standard* DTI). Results for the N1 component showed main effects of sound [$F(1, 13) = 81.90$, $p < 0.0001$], phase [$F(1, 13) = 63.79$, $p < 0.0001$], ROI [$F(5, 65) = 81.69$, $p < 0.0001$] and Model [$F(7, 91) = 92.96$, $p < 0.0001$]. The model effect was better qualified by

significant interactions between Phase and Model [$F(7, 91) = 15.84$, $p < 0.001$] and Sound and Model [$F(7, 91) = 7.67$, $p < 0.0001$]. Univariate ANOVAs were performed to investigate the Phase effect and Sound effect for each head model. Only the Concentric sphere model showed a significant Phase effect, with larger post-tetanzation than pre-tetanzation activity (Fig. 9, left panel).

We compared the effect of our experimental condition on the P2 AEP source solutions obtained with the several head models under investigation. Results of the P2 AEP component showed significant main effects of Sound [$F(1, 13) = 18.30$, $p < 0.0001$], Phase [$F(1, 13) = 32.45$, $p < 0.0001$], and ROI [$F(5, 65) = 84.46$, $p < 0.0001$]. The main effect of Model [$F(7, 91) = 89.19$, $p < 0.0001$] was better qualified by the significant interactions between Phase and Model [$F(7, 91) = 13.28$, $p < 0.0001$], and Sound and Model [$F(7, 91) = 33.44$, $p < 0.0001$]. p -values of the simple effects are reported in Table 2. The effects were significant for all head models. Concentric sphere, 4-FEMmeshCSF, and 9-FEMmesh *Standard* DTI were the models that explained the highest variance for the Sound and Phase effects. (Fig. 10, middle and right panels).

The solution obtained with all head models were compared each other by computing correlational values. Results of this correlational approach are displayed in Fig. 11. CDR values ± 40 ms from the peak of the N1 component were averaged cross experimental conditions and ROIs for each head model. Pearson correlations were significant for each model pair (r 's > 0.81 , p 's < 0.0001). The correlation heatmap suggests weaker correlations

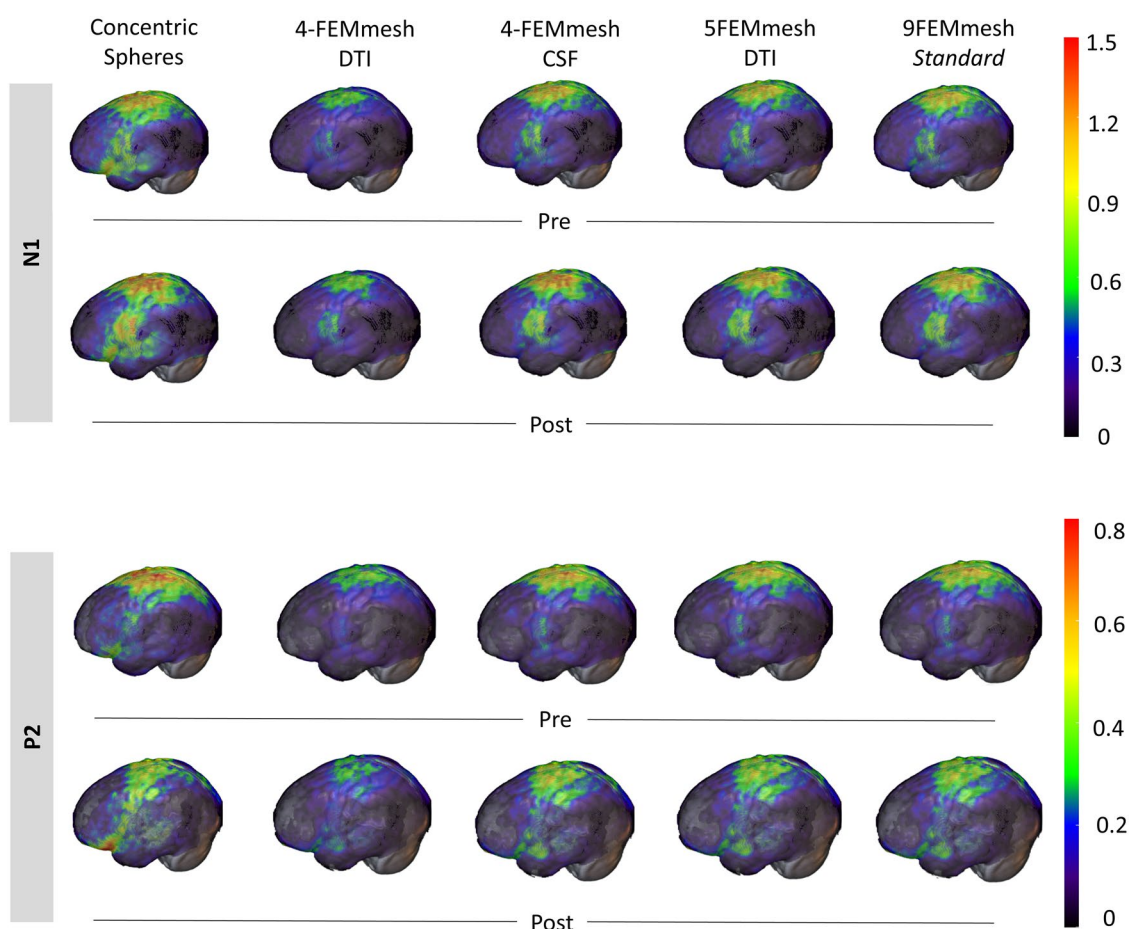


Fig. 9 Sagittal view of 3D renderings of the CDR values around the peak of the N1 (top) and P2 (bottom) ERP components as a function of Phase across five selected head models. The grand average activity is plotted on a 20–24 years average template. All model solutions

show an increased N1 and P2 activity during the post-tetanzing phase over temporal areas. A more widespread activity resulted from the concentric sphere model compared to the remaining models

Table 2 P-values and eta-squared values of the Phase effect for both N1 and P2 AEP components, and Sound effect for the P2 AEP component

Model	Phase N1		Phase P2		Sound P2	
	<i>p</i>	η^2	<i>p</i>	η^2	<i>p</i>	η^2
Concentric sphere	0.0096	0.415	0.0014	0.555	0.0061	0.450
BEM dipoli	0.0582	0.249	0.0027	0.511	0.0272	0.322
3-compartment	0.0977	0.197	0.0037	0.489	0.0189	0.356
4-FEMmesh CSF	0.0764	0.222	0.0032	0.500	0.0176	0.362
4-FEMmesh DTI	0.0928	0.202	0.0033	0.498	0.0201	0.350
5-FEMmesh DTI	0.0755	0.223	0.0028	0.509	0.0205	0.348
9-FEMmesh <i>Standard</i>	0.0851	0.211	0.0025	0.518	0.0193	0.353
9-FEMmesh DTI	0.0825	0.214	0.0022	0.525	0.0210	0.346

All head models showed an increased in the CDR activity after the tetanizing phase and higher CDR response for the 1 k Hz sound. Statistically significant changes are reported in bold

between the simple models (i.e., Concentric Sphere and BEM dipoli models) and all the other head models. Furthermore, stronger correlations with complex head models

(e.g., 5-FEMmesh and 9-FEMmesh models) derived by the inclusion of the CSF compared with both isotropic and anisotropic solutions of the 4-FEMmesh models.

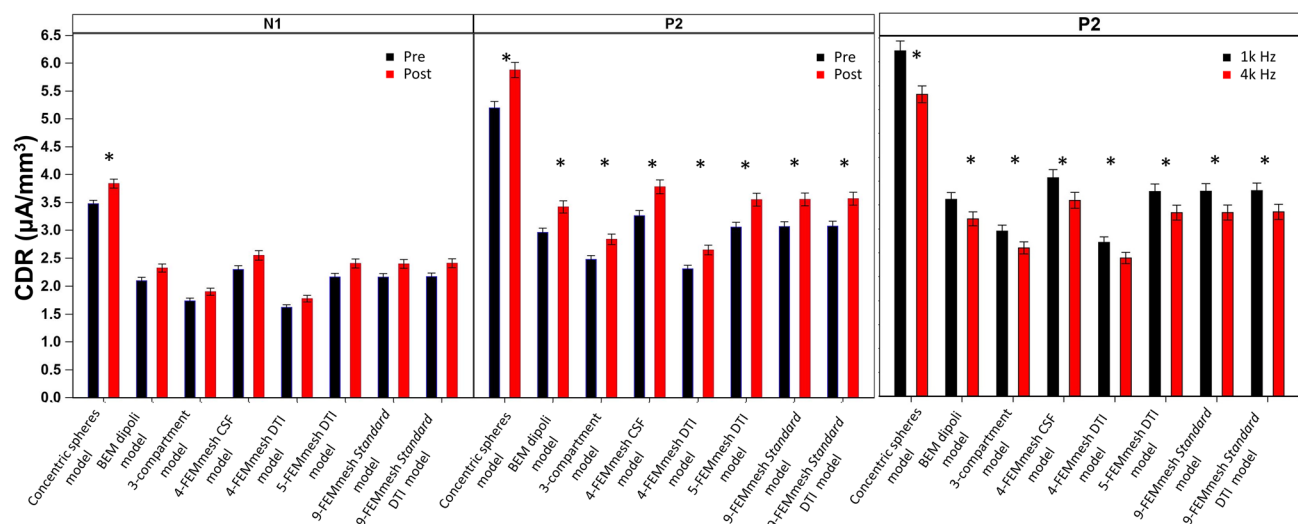


Fig. 10 CDR values around the peak of the N1 and P2 components for the pre- and post-tetanizing phase (left and middle panels) and for the Sound types (left panel) across models. Significant differences are marked with *

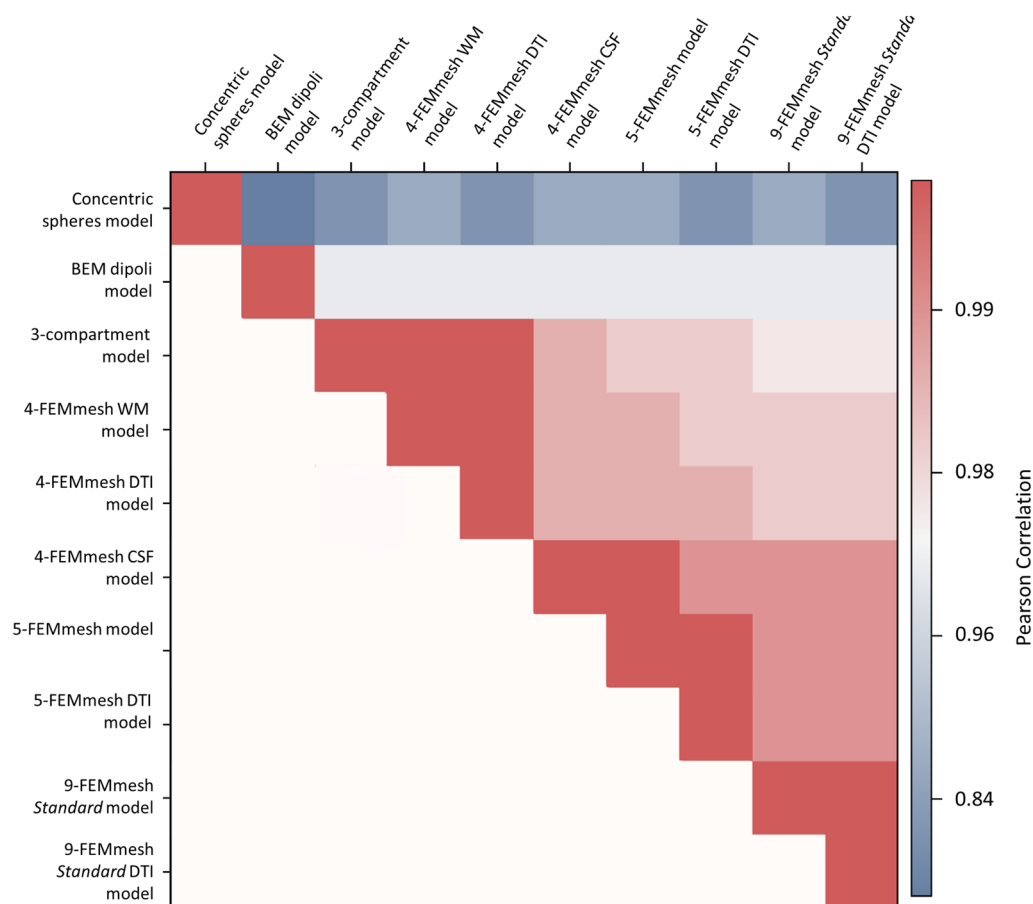


Fig. 11 Correlation matrix of CDR values around the N1 peak across auditory areas for all the considered head models. Concentric sphere and BEM dipoli solutions show weak correlations with all the

remaining models. The solution obtained modeling the CSF strongly correlated with the solution obtained with more realistic head models (i.e., isotropic and anisotropic 9-FEMmesh models)

Comparable source solution to the most realistic head models is obtained from modeling the CSF.

We further compared the source solutions of the different head models calculating the relative change across ROIs between a reference solution (either isotropic, i.e., 9-FEMmesh *Standard* or anisotropic, i.e., 5-FEMmesh DTI) and the solutions obtained with all the remaining models. The relative change is expressed as the ratio between each model and the reference solution considering the absolute CDR values of the grand average N1 component across auditory ROIs. Low values indicate a smaller change between the source solution of a given model to the reference model (i.e., high similarity). Results are visually reported in Fig. 12 as ogive curves of the cumulative frequency distributions. The CDR distribution obtained with the Concentric Sphere model differed from both the considered reference solutions. On the other hand, the inclusion of the CSF had a big influence and produced similar CDR distributions to the reference models. The difference in the solution obtained by modeling WM anisotropy (aqua line) in the 4-FEMmesh model (purple line) was trivial compared with the solution obtained by modeling the CSF (green line).

Finally, we calculated the distance between the peak in source activity obtained with the 9-FEMmesh *Standard* solution and all remaining models. Details of this comparison are reported in the Supplementary Material. The Concentric Sphere and BEM dipoli models showed their

maximum CDR activity further away from the solution obtained with the reference model (Figures S2a and S2b).

Isotropic and Anisotropic Model Comparison

We compared the solutions obtained with and without modeling WM anisotropic values to gain insight into the impact of WM anisotropy on EEG source localization. A univariate ANOVA on the CDR values for the grand average data around the peak of N1 and P2 components was performed for each head model including the WM compartment (i.e., 4-FEMmesh, 5-FEMmesh, and 9-FEMmesh *Standard*). CDR values for isotropic and anisotropic solutions of each AEP component are depicted in Fig. 8 as a function of head model. Overall, the 4-FEMmesh solutions provided the smaller CDR activity compared to the other more complex models (i.e., 5-FEMmesh and 9-FEMmesh). Moreover, similar source solutions were obtained by modeling isotropic and anisotropic WM characteristics for all head models. The comparison between isotropic and anisotropic solutions for each head model showed nonsignificant differences in the N1 source [$F_s(1, 2) < 0.05$, p 's > 0.8206]. Nonsignificant differences were obtained comparing models for the source of the P2 component [$F_s(1, 2) < 0.16$, p 's > 0.6914].

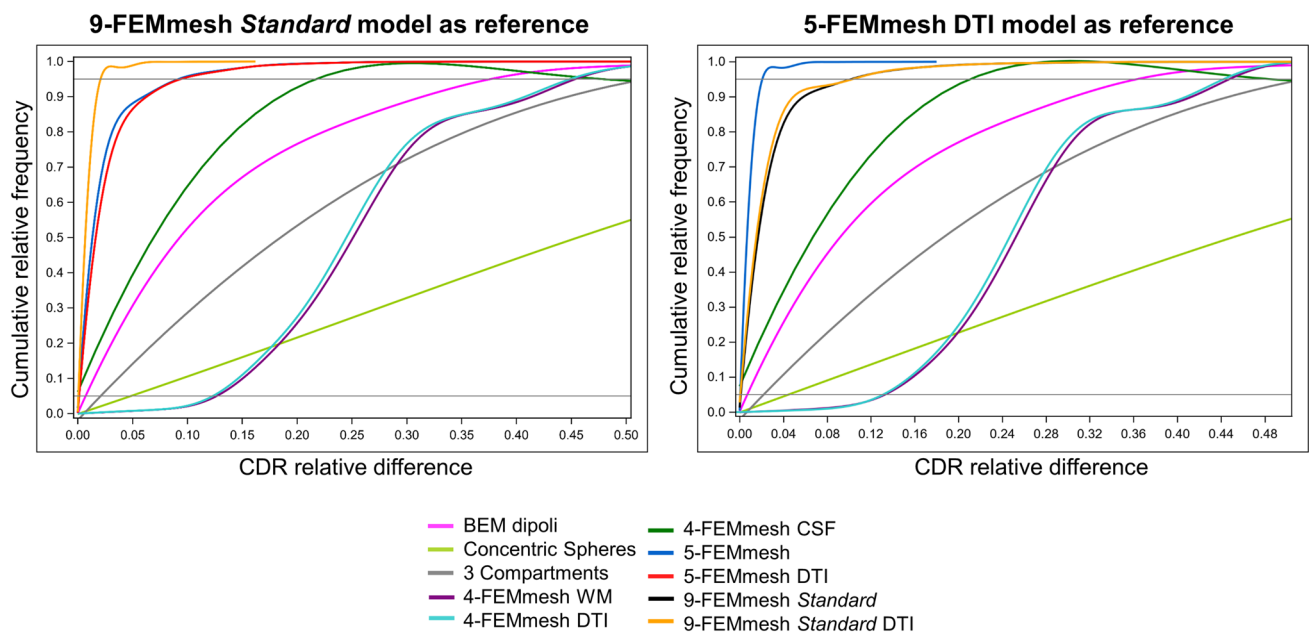


Fig. 12 Cumulative relative frequency of the relative change in the CDR obtained with the different head models. Left panel represent the difference of CDR values across auditory ROIs obtained for each head model relative to the standard model. Right panel shows the dif-

ference in the source solution of each model relative to the 5-compartment DTI model. The horizontal grey lines represent 5% and 95% of cumulative relative frequency

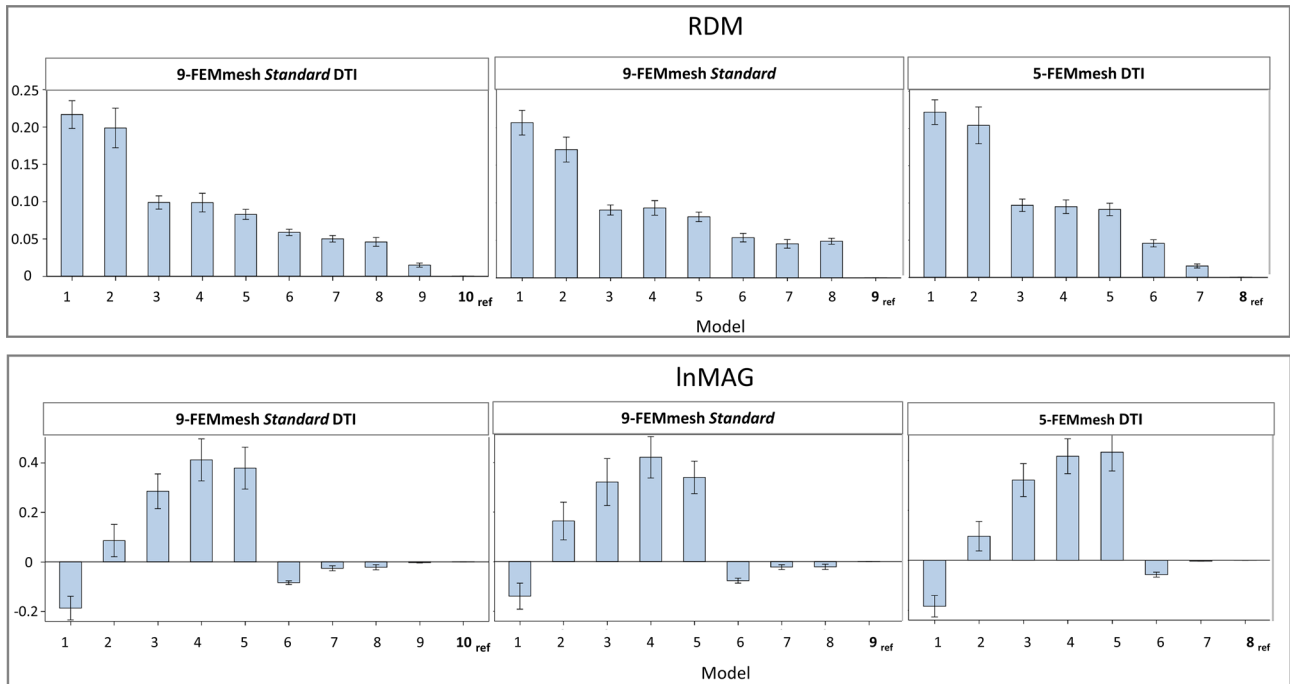


Fig. 13 RDM (top) and lnMAG (bottom) values of the comparison between three base models (i.e., Standard DTI, Standard, and 5-compartment DTI models) and all the other head models obtained from simulated data. Low RDM values (top panels) indicates that the solution obtained with the model is close to the solution obtained with the base model. Magnitude values (bottom panels) represent the difference in magnitude obtained with each solution compared to the base

model. Positive values suggest an increase in magnitude. Negative values suggest a reduction in the magnitude of the solution. Model labels: Model 1: Concentric Spheres, Model 2: BEM dipoli, Model 3: 3-compartment, Model 4: 4-FEMmesh WM, Model 5: 4-FEMmesh DTI, Model 6: 4-FEMmesh CSF, Model 7: 5-FEMmesh, Model 8: 5-FEMmesh DTI, Model 9: 9-FEMmesh Standard, and Model 10: 9-FEMmesh Standard DTI

Simulated EEG from Source

We selected the CDR values from the primary auditory areas (bilateral A1 core, A1 caudal, and A1 rostral) to perform a simulation of the EEG activity on the scalp. We calculated an EEG forward solution starting from the CDR values of the auditory and visual areas for each head model. We calculated two indices utilized in previous similar studies, i.e., the relative difference measure (RDM) and the logarithmic magnitude difference (lnMAG) (Lee et al. 2009; Vorwerk et al. 2014) to qualify the difference in the forward solutions obtained with the different head models. The RDM quantifies the numerical error in the topography of the electrical field and it was computed as follow:

$$RDM = \sqrt{\sum_{i=1}^n \left(\frac{mod_x}{\sqrt{\sum_{i=1}^n (mod_x)^2}} - \frac{ref_x}{\sqrt{\sum_{i=1}^n (ref_x)^2}} \right)^2}$$

RDM values close to zero indicate that the solution provided similar topographical distribution to the reference model. The second measure is a calculation of the potential magnitude error of each head model (mod_x) compared to the reference solution (ref_x).

$$lnMAG = \log \sqrt{\frac{\sum_{i=1}^n (mod_x)^2}{\sum_{i=1}^n (ref_x)^2}}$$

Negative lnMAG values suggest an increase in the strength on the magnitude for the one solution compared to the reference model. RDM and lnMAG are complementary measures, thus a complete picture can be drawn by considering the results provided by both these indices together. Figure 13 depicts the RDM (top panels) and lnMAG (bottom panels) of simulated data as a function of head model, separately for each model used as reference. Low RDM and lnMAG values were obtained for both 5-FEMmesh models and 4-FEMmesh CSF model. The Concentric Sphere solution showed larger magnitude than each of the reference models, as indicated by negative lnMAG values. However, when the RDM index is taken into account, the solution

from the Concentric Sphere model showed the biggest difference in signal topography.

In line with these results the scalp activity obtained from the forward solution with the Concentric Sphere model resembled less the recorded N1 scalp distribution than the remaining models. An example of scalp distribution from a representative participant is depicted in Figure S3.

Discussion

One aim of our study was to investigate the effect of auditory tetanization on the N1 and P2 AEP and their cortical sources in healthy young adult participants. We found LTP-like effect on the N1 component in the form of specific increased amplitude in response to the 1 k Hz sound (i.e., tetanus) few minutes after the tetanic stimulation. Nonsignificant tetanizing effects were found for the amplitude of the P2 AEP. The neural generators of both AEPs were localized in areas of the primary auditory cortex with larger activity recorded in the left hemisphere due to our monaural presentation of the stimuli (i.e., right ear).

Both EEG and fMRI results suggest that the tetanizing effects produced by sensory stimulation can induce a long-lasting change due to LTP-caused cortical plasticity in the auditory cortex. Clapp et al. (2005) showed that high-frequency repetition of 1000-Hz bursts can induce an auditory LTP-like effect in healthy adult participants. The potentiation effect was recorded over fronto-central regions of the scalp and lasted for over 1 h after the tetanizing phase (Clapp et al. 2005). The examination of brain plasticity has been applied to investigate the neural basis of neuropsychiatric disorders, such as schizophrenia. Mears and Spencer (2012) investigated the differences in the potentiation effect both right after and about 20 min after tetanic stimulation, using an oddball task with two standard tones. No potentiation effect was evident in schizophrenia patients during the first recording after the tetanic phase, while healthy controls showed a stimulus-specific plasticity effect over right lateral temporal electrodes. This initial effect was recorded over frontal electrodes in the control group and over right frontotemporal electrodes in patients approximately 20 min after the stimulation (Mears and Spencer 2012). Recently, auditory LTP-like effects were elicited on the N1 AEP by a broader range of stimuli in healthy young adults. Specifically, pure-tones, narrow-band noise, and white noise stimuli showed to induce LTP-like potentiation effects for over one hour when presented in a tetanic fashion (Lei et al. 2017). Moreover, the potentiation effect produced by auditory tetanic stimulation is modulated by participant's attention and age. In young adults post-tetanization P2 and N2 amplitudes, but not N1 amplitudes, were larger during active than

passive listening. Only P2 amplitudes were enhanced during active listening in older adults (Harris et al. 2012).

The N1 and P2 activities recorded during our experimental procedure were detected in electrodes placed on the fronto-central regions of the scalp. We found significant tetanizing effects on the N1, but not P2 component, consistent with prior work. The N1 amplitude increased in response to the 1 k Hz tones after the tetanizing stimulation. This tetanizing effect was detected over central and fronto-central electrodes. Nonsignificant changes were recorded on the N1 response to 4 k Hz tone bursts. The effect of the tetanizing stimulation did not extend to the P2 AEP. It is possible that the passive listening nature of our task reduced the tetanizing modulation of the P2 component (Harris et al. 2012), which could have been detected if participants were actively involved in a sound-detection task. The standard head model utilized in previous studies of our lab, i.e., 9-FEM *Standard*, was found to detect differences between the pre- and post-tetanizing phases in the source of the N1 component. Moreover, the neural generator of the N1 activity seemed to be localized in the core and rostral areas of the Heschl's gyrus. Similar results have been obtained for the P2 source. Interestingly, the source reconstructed data revealed areas of activity in regions far from the auditory cortex (e.g., posterior cingulate cortex, insula). However, the activity of these areas was unrelated to our auditory experimental manipulations and did not appear in the condition difference CDR maps (Fig. 5). There were several areas of activity found in the distributed source analysis possibly reflecting cognitive or brain processes unrelated to our auditory manipulations. This result is partially different from source analysis results obtained in simulation studies, where a point-like source is defined a priori. Results of source analysis with experimental datasets are sensitive to additional brain areas that might be involved in unrelated activity to the experimental manipulation (e.g., silent reading for our experiment). However, only restricted areas show specific sensitivity to the experimental manipulation. Our study is the first to systematically investigate the tetanizing effect at the source level. Results are in line with evidence on the LTP-like changes in the hemodynamic response of the auditory cortex in humans. In a fMRI study, the BOLD signal in the primary auditory cortices showed potentiation effects after the binaural presentation of an auditory tetanus (Zaehle et al. 2007).

An additional aim of our study was to compare the effect of modeling different head compartments, including either isotropic and anisotropic values of WM, and applying different forward methods on the source reconstruction of AEPs. We performed several quantitative and qualitative comparisons of the different solutions of source analysis. Overall, the inclusion of the CSF provided similar solutions to the ones obtained with complex head representations. Instead,

modeling the WM anisotropy showed less similar source solutions of AEPs to more complex head models.

Our results on simulated data supported the importance of the inclusion of the CSF in the head model for source reconstruction. The solution obtained modeling the CSF was topographically similar to the solutions of more complex models, when the CDR values of areas in the primary auditory cortex are used to calculate EEG forward solutions. On the other hand, the solution obtained with the simplest model (i.e., Concentric Sphere) was characterized by high magnitude values but large localization errors when compared with more realistic head representations (Fig. 13). Together these results suggest that modeling the CSF is sufficient to achieve similar source solutions to the ones provided by complex head representations.

Findings from several simulation studies converge in concluding that neglecting the CSF geometry and conductivity provides inaccurate reconstruction of scalp distributions (Ramon et al. 2004) and leads to larger localization errors (Ramon et al. 2006; Wendel et al. 2008). The diffusion coefficients in the CSF are larger than in the brain, thus neglecting this distinction introduces errors in the reconstruction of the neural sources (Wolters et al. 2006) especially for superficial sources (Vorwerk et al. 2014). The CSF has a complex geometry since it fills both the subarachnoid space (i.e., superficial CSF) and ventricles in the brain (i.e., interior CSF). However, the interior CSF seems to influence the localization error of deep sources (Lanfer et al. 2012), thus a simplified head model such as the BEM models with the inclusion of only the superficial CSF would provide negligible source localization errors (Wolters et al. 2006).

A further step in considering realistic head models for source analysis implies the inclusion of electrical anisotropy of certain tissues. The WM is known for its property of conducting electrical current in preferential directions (i.e., anisotropic conductivity) rather than equally in all directions (i.e., isotropic conductivity). Modeling the WM anisotropy in our study showed to produce more similar source solutions to the complex models, but negligible differences were found between isotropic and anisotropic solutions of the same head model (Figs. 8, 10, and 11). Results of previous simulation studies found that the inclusion of WM anisotropy influences source magnitude and orientation but has a less influence on source localization errors (Güllmar et al. 2010; Haueisen et al. 2002; Neugebauer et al. 2017). Introducing WM anisotropy for deep sources that are close to the WM compartment provides source solutions that are less sensitive to topographic errors (Vorwerk et al. 2014; Wolters et al. 2006). Our findings on experimental data are in line with the results of simulation studies and suggest that cortical sources of AEPs are largely influenced by modeling the CSF compartment. The results of simplified head representations (i.e., 4-FEM-mesh models) are equivalent to more

complex head models (e.g., 5- and 9-FEM-mesh models) when the CSF is included in the head model. Modeling WM anisotropy seems to be less important than including the CSF, thus it might be omitted with negligible effects on the localization error of superficial auditory sources.

Bangera et al. (2010) draw similar conclusions with data from patients with epilepsy after comparing models of different complexity with the gold standard measure of intracranial EEG activity. They found the greatest improvement by modeling the WM anisotropy when the stimulation site was close to a region of high anisotropy. The best anisotropic model considers the linear scaling of the eigenvalues of the WM tensor (i.e., equivalent to our DTI approach) instead of taking into account only the eigenvalues tangential to the fiber direction. However, changes in the topography distribution of reconstructed sources are not as drastic when WM anisotropy is modeled along with the CSF (Bangera et al. 2010). Similar conclusions have been obtained comparing EEG sources and fMRI cortical activations elicited by visual stimuli. The accuracy in EEG source localization of visual evoked potentials showed to be slightly improved by the modeling of WM anisotropy. Comparable solutions were obtained from isotropic and anisotropic models when compared with the fMRI activations in the primary visual cortex (Lee et al. 2009). One difference with our study is that in Bangera et al. (2010)—similarly to simulation studies—the EEG generators were known a priori and localized source could be modeled. Our approach drew similar conclusions about the complexity and characteristics of the head model, even though we based our analyses on distributed source models.

A common thread of our results is that the complexity of the head representation plays an important role in the source analysis solutions. Results of the correlational approach showed large differences in the topographical distribution of the N1 source obtained with the concentric spheres and BEM-dipoli models and all the remaining models. On the other hand, modeling the CSF made the 4-FEMmesh model solution similar to solutions of more complex head representations (i.e., 5- and 9-FEMmesh models; Fig. 11). Similar conclusions can be drawn from the distribution of cumulative relative frequencies (Fig. 12). The ogive distribution of the 4-FEMmesh CSF was closer to the distribution of the 5-FEMmesh, and 9-FEMmesh models, suggesting a similar pattern in the solution of these models to either reference models (i.e., 9-FEMmesh *Standard* or 5-FEMmesh DTI). The source solution of less complex models provided a dissimilar distribution of the CDR values to the reference models, with the worst result obtained with the Concentric spheres model. This evidence suggests that a simplification of the head in concentric spheres with isotropic conductivity values might lead to widespread source solutions. Simplified

spherical shell models neglect the complex anatomy of the head and provide less realistic solutions. Furthermore, results of the model comparisons in relation to the experimental factors of our study (i.e., Sound and Phase) suggested that significant effects can be detected with different head models, with the Concentric Sphere model showing large and widespread CDR values.

These results further confirm that the use of simplistic representations of the head may mislocate the effects of experimental manipulations.

Numerous studies have used computer simulations to investigate the role of modeling different head compartments as well as introducing anisotropic and inhomogeneous parameters for EEG forward and inverse solutions. Findings suggest that the performance of a more complex head model is higher than a solution in which less compartments are modeled. Considerable error is introduced by neglecting the CSF and the WM and GM distinction (Neugebauer et al. 2017; Vorwerk et al. 2014).

Overall, results of the current study extend the literature on the auditory LTP-like effect in healthy adult participants by suggesting that tetanizing effects affect cortical components of the AEPs localized in the primary auditory cortex. Moreover, EEG source localization in experimental protocols seems to be sensitive to the use of realistic head models that include the CSF compartment. Modeling WM anisotropy has a negligible effect on the localization of cortical sources, but it might improve the source solution for deeper sources. Further experimental studies should be performed to evaluate the effect of WM anisotropic conductivity on the localization of deep brain sources. The use of complex head models that resemble a realistic head representation are recommended for accurate source localization of EEG signals.

Supplementary Information The online version contains supplementary material available at <https://doi.org/10.1007/s10548-021-00871-z>.

Acknowledgements This research was supported by the National Institute of Child Health and Human Development (NICHD) of the National Institute of Health under award numbers R01-HD18942 and K99-HD102566.

Funding National Institute of Child Health and Human Development (NICHD) R01-HD18942 and K99-HD102566.

Data Availability The datasets generated during and/or analyzed during the current study are available from the corresponding author on reasonable request.

Declarations

Conflict of interest The authors declare no personal or institutional conflict of interests.

References

- Andersson JLR, Sotiropoulos SN (2016) An integrated approach to correction for off-resonance effects and subject movement in diffusion MR imaging. *Neuroimage* 125:1063–1078. <https://doi.org/10.1016/j.neuroimage.2015.10.019>
- Andersson JL, Skare S, Ashburner J (2003) How to correct susceptibility distortions in spin-echo echo-planar images: application to diffusion tensor imaging. *Neuroimage* 20(2):870–888. [https://doi.org/10.1016/S1053-8119\(03\)00336-7](https://doi.org/10.1016/S1053-8119(03)00336-7)
- Bangera N, Schomer D, Dehghani N, Ulbert I, Cash S, Papavasiliou S et al (2010) Experimental validation of the influence of white matter anisotropy on the intracranial EEG forward solution. *J Comput Neurosci* 29(3):371–387. <https://doi.org/10.1007/s10827-009-0205-z>
- Basser PJ, Mattiello J, LeBihan D (1994) MR diffusion tensor spectroscopy and imaging. *Biophys J* 66(1):259–267. [https://doi.org/10.1016/S0006-3495\(94\)80775-1](https://doi.org/10.1016/S0006-3495(94)80775-1)
- Bigdely-Shamlo N, Mullen T, Kothe C, Su K-M, Robbins KA (2015) The PREP pipeline: standardized preprocessing for large-scale EEG analysis. *Front Neuroinform* 9:16. <https://doi.org/10.3389/fninf.2015.00016>
- Biront G, Spinelli L, Vulliémaz S, Mégevand P, Brunet D, Seeck M, Michel CM (2014) Head model and electrical source imaging: a study of 38 epileptic patients. *NeuroImage Clin* 5:77–83
- Buzzell GA, Richards JE, White LK, Barker TV, Pine DS, Fox NA (2017) Development of the error-monitoring system from ages 9–35: unique insight provided by MRI-constrained source localization of EEG. *Neuroimage* 2017:13–26. <https://doi.org/10.1016/j.neuroimage.2017.05.045>
- Cho JH, Vorwerk J, Wolters CH, Knosche TR (2015) Influence of the head model on EEG and MEG source connectivity analyses. *Neuroimage* 110:60–77. <https://doi.org/10.1016/j.neuroimage.2015.01.043>
- Clapp WC, Kirk IJ, Hamm JP, Shepherd D, Teyler TJ (2005) Induction of LTP in the human auditory cortex by sensory stimulation. *Eur J Neurosci* 22(5):1135–1140. <https://doi.org/10.1111/j.1460-9568.2005.04293.x>
- Conte S, Richards JE, Guy MW, Xie W, Roberts JE (2020) Face-sensitive brain responses in the first year of life. *Neuroimage* 211:116602. <https://doi.org/10.1016/j.neuroimage.2020.116602>
- Delorme A, Makeig S (2004) EEGLAB: an open source toolbox for analysis of single-trial EEG dynamics including independent component analysis. *J Neurosci Methods* 134(1):9–21. <https://doi.org/10.1016/j.jneumeth.2003.10.009>
- Delorme A, Sejnowski T, Makeig S (2007) Enhanced detection of artifacts in EEG data using higher-order statistics and independent component analysis. *Neuroimage* 34(4):1443–1449. <https://doi.org/10.1016/j.neuroimage.2006.11.004>
- Eickhoff SB, Paus T, Caspers S, Grosbras M-H, Evans AC, Zilles K, Amunts K (2007) Assignment of functional activations to probabilistic cytoarchitectonic areas revisited. *Neuroimage* 36(3):511–521. <https://doi.org/10.1016/j.neuroimage.2007.03.060>
- Fillmore PT, Richards JE, Phillips-Meek MC, Cryer A, Stevens M (2015) Stereotaxic magnetic resonance imaging brain atlases for infants from 3 to 12 months. *Dev Neurosci* 37(6):515–532. <https://doi.org/10.1159/000438749>
- Gao C, Conte S, Richards JE, Xie W, Hanayik T (2019) The neural sources of N170: understanding timing of activation in face-selective areas. *Psychophysiology*. <https://doi.org/10.1111/psyp.13336>
- Güllmar D, Haueisen J, Reichenbach JR (2010) Influence of anisotropic electrical conductivity in white matter tissue on the EEG/MEG forward and inverse solution. A high-resolution whole head

- simulation study. *Neuroimage* 51(1):145–163. <https://doi.org/10.1016/j.neuroimage.2010.02.014>
- Hallez H, Vanrumste B, Grech R, Muscat J, De Clercq W, Vergult A et al (2007) Review on solving the forward problem in EEG source analysis. *J Neuroeng Rehabil* 4:46. <https://doi.org/10.1186/1743-0003-4-46>
- Hallez H, Staelens S, Lemahieu I (2009) Dipole estimation errors due to not incorporating anisotropic conductivities in realistic head models for EEG source analysis. *Phys Med Biol* 54(20):6079–6093. <https://doi.org/10.1088/0031-9155/54/20/004>
- Harris KC, Wilson S, Eckert MA, Dubno JR (2012) Human evoked cortical activity to silent gaps in noise: effects of age, attention, and cortical processing speed. *Ear Hear* 33(3):330. <https://doi.org/10.1097/AUD.0b013e31823fb585>
- Hauelsen J, Tuch DS, Ramon C, Schimpf PH, Wedeen VJ, George JS, Belliveau JW (2002) The influence of brain tissue anisotropy on human EEG and MEG. *Neuroimage* 15(1):159–166. <https://doi.org/10.1006/nimg.2001.0962>
- Jatoi MA, Kamel N, Malik AS, Faye I (2014) EEG based brain source localization comparison of sLORETA and eLORETA. *Australas Phys Eng Sci Med* 37(4):713–721
- Jung T-P, Makeig S, Humphries C, Lee T-W, McKeown MJ, Iragui V, Sejnowski TJ (2000) Removing electroencephalographic artifacts by blind source separation. *Psychophysiology* 37(2):163–178. <https://doi.org/10.1111/1469-8986.3720163>
- Lanfer B, Scherg M, Dannhauer M, Knösche TR, Burger M, Wolters CH (2012) Influences of skull segmentation inaccuracies on EEG source analysis. *Biomed Tech (berl)* 57:623–626. <https://doi.org/10.1515/bmt-2012-4020>
- Lee WH, Liu Z, Mueller BA, Lim K, He B (2009) Influence of white matter anisotropic conductivity on EEG source localization: comparison to fMRI in human primary visual cortex. *Clin Neurophysiol* 120(12):2071–2081. <https://doi.org/10.1016/j.clinph.2009.09.007>
- Lei G, Zhao Z, Li Y, Yu L, Zhang X, Yan Y et al (2017) A method to induce human cortical long-term potentiation by acoustic stimulation. *Acta Otolaryngol* 137(10):1069–1076. <https://doi.org/10.1080/00016489.2017.1332428>
- Lopez-Calderon J, Luck SJ (2014) ERPLAB: an open-source toolbox for the analysis of event-related potentials. *Front Hum Neurosci* 8:213. <https://doi.org/10.3389/fnhum.2014.00213>
- Mears RP, Spencer KM (2012) Electrophysiological assessment of auditory stimulus-specific plasticity in schizophrenia. *Biol Psychiatry* 71(6):503–511. <https://doi.org/10.1016/j.biopsych.2011.12.016>
- Michel CM, Brunet D (2019) EEG source imaging: a practical review of the analysis steps. *Front Neurol* 10:325. <https://doi.org/10.3389/fneur.2019.00325>
- Michel CM, Murray MM (2012) Towards the utilization of EEG as a brain imaging tool. *Neuroimage* 61(2):371–385. <https://doi.org/10.1016/j.neuroimage.2011.12.039>
- Michel CM, Murray MM, Lantz G, Gonzalez S, Spinelli L, Grave de Peralta R (2004) EEG source imaging. *Clin Neurophysiol* 115(10):2195–2222. <https://doi.org/10.1016/j.clinph.2004.06.001>
- Michel CM, Koenig T, Brandeis D, Gianotti LRR, Wackermann J (2009) *Electrical neuroimaging*. Cambridge University Press, Cambridge
- Morosan P, Rademacher J, Schleicher A, Amunts K, Schormann T, Zilles K (2001) Human primary auditory cortex: cytoarchitectonic subdivisions and mapping into a spatial reference system. *Neuroimage* 13(4):684–701. <https://doi.org/10.1006/nimg.2000.0715>
- Neugebauer F, Moddel G, Ramm P, Burger M, Wolters CH (2017) The effect of head model simplification on beamformer source localization. *Front Neurosci* 11:625. <https://doi.org/10.3389/fnins.2017.00625>
- Oostendorp TF, van Oosterom A (1989) Source parameter estimation in inhomogeneous volume conductors of arbitrary shape. *IEEE Trans Biomed Eng* 36(3):382–391. <https://doi.org/10.1109/10.19859>
- Oostenveld R, Fries P, Maris E, Schoffelen JM (2011) FieldTrip: open source software for advanced analysis of MEG, EEG, and invasive electrophysiological data. *Comput Intell Neurosci* 2011:156869. <https://doi.org/10.1155/2011/156869>
- Pascual-Marqui RD, Pascual-Montano AD, Lehmann D, Kochi K, Esslen M, Jancke L, Anderer P, Saletu B, Tanaka H, Hirata K, John ER, Prichep L (2006) Exact low resolution brain electromagnetic tomography (eLORETA). *Neuroimage* 31(Suppl. 1):S86
- Pascual-Marqui RD, Lehmann D, Koukoku M, Kochi K, Anderer P, Saletu B et al (2011) Assessing interactions in the brain with exact low-resolution electromagnetic tomography. *Philos Trans R Soc Lond A* 369(1952):3768–3784. <https://doi.org/10.1098/rsta.2011.0081>
- Pascual-Marqui RD (2007) Discrete, 3D distributed, linear imaging methods of electric neuronal activity. Part 1: exact, zero error localization. Retrieved from <http://arxiv.org/abs/0710.3341>. Accessed 31 July 2020
- Ramon C, Schimpf P, Hauelsen J, Holmes M, Ishimaru A (2004) Role of soft bone, CSF and gray matter in EEG simulations. *Brain Topogr* 16:245–248
- Ramon C, Schimpf PH, Hauelsen J (2006) Influence of head models on EEG simulations and inverse source localizations. *Biomed Eng Online* 5:10. <https://doi.org/10.1186/1475-925X-5-10>
- Richards JE (2013) Cortical sources of ERP in prosaccade and anti-saccade eye movements using realistic source models. *Front Syst Neurosci* 7:27. <https://doi.org/10.3389/fnsys.2013.00027>
- Richards JE, Xie W (2015) Brains for all the ages: structural neurodevelopment in infants and children from a life-span perspective. *Adv Child Dev Behav* 48:1–52. <https://doi.org/10.1016/bs.acdb.2014.11.001>
- Richards JE, Sanchez C, Phillips-Meek M, Xie W (2015) A database of age-appropriate average MRI templates. *Neuroimage* 124(Pt B):1254–1259. <https://doi.org/10.1016/j.neuroimage.2015.04.055>
- Richards JE, Gao C, Conte S, Guy M, Xie W (2018) Supplemental information for the neural sources of N170: understanding timing of activation in face-selective areas. Retrieved from <https://wp.me/a9YKYg-fm>. Accessed 31 July 2020
- Russell GS, Jeffrey Eriksen K, Poolman P, Luu P, Tucker DM (2005) Geodesic photogrammetry for localizing sensor positions in dense-array EEG. *Clin Neurophysiol* 116(5):1130–1140. <https://doi.org/10.1016/j.clinph.2004.12.022>
- Sanders PJ, Thompson B, Corballis PM, Maslin M, Searchfield GD (2018) A review of plasticity induced by auditory and visual tetanic stimulation in humans. *Eur J Neurosci* 48(4):2084–2097. <https://doi.org/10.1111/ejn.14080>
- Shattuck DW, Mirza M, Adisetiyo V, Hojatkashani C, Salamon G, Narr KL et al (2008) Construction of a 3D probabilistic atlas of human cortical structures. *Neuroimage* 39(3):1064–1080. <https://doi.org/10.1016/j.neuroimage.2007.09.031>
- Smith SM, Jenkinson M, Woolrich MW, Beckmann CF, Behrens TEJ, Johansen-Berg H et al (2004) Advances in functional and structural MR image analysis and implementation as FSL. *Neuroimage* 23:S208–S219. <https://doi.org/10.1016/j.neuroimage.2004.07.051>
- Tuch DS, Wedeen VJ, Dale AM, George JS, Belliveau JW (2001) Conductivity tensor mapping of the human brain using diffusion tensor MRI. *Proc Natl Acad Sci USA* 98(20):11697–11701. <https://doi.org/10.1073/pnas.171473898>
- Tucker DM (1993) Spatial sampling of head electrical fields—the geodesic sensor net. *Electroencephalogr Clin Neurophysiol* 87(3):154–163. [https://doi.org/10.1016/0013-4694\(93\)90121-B](https://doi.org/10.1016/0013-4694(93)90121-B)

- Tucker DM, Liotti M, Potts GF, Russell GS, Posner MI (1994) Spatiotemporal analysis of brain electrical fields. *Hum Brain Mapp* 1(2):134–152. <https://doi.org/10.1002/hbm.460010206>
- Vatta F, Meneghini F, Esposito F, Mininell S, Di Salle F (2010) Realistic and spherical head modeling for EEG forward problem solution: a comparative cortex-based analysis. *Comput Intell Neurosci*. <https://doi.org/10.1155/2010/972060>
- Vorwerk J, Cho JH, Rampp S, Hamer H, Knosche TR, Wolters CH (2014) A guideline for head volume conductor modeling in EEG and MEG. *Neuroimage* 100:590–607. <https://doi.org/10.1016/j.neuroimage.2014.06.040>
- Vorwerk J, Oostenveld R, Piastra MC, Magyari L, Wolters CH (2018) The FieldTrip-SimBio pipeline for EEG forward solutions. *Biomed Eng Online* 17(1):37. <https://doi.org/10.1186/s12938-018-0463-y>
- Vorwerk J, Magyari L, Ludewig J, Oostenveld R, & Wolters CH (2013) The fieldtrip-simbio pipeline for finite element EEG forward computations in MATLAB: validation and application. T. Paper presented at the International Conference on Basic and Clinical Multimodal Imaging. Geneva, Switzerland
- Wendel K, Narra NG, Hannula M, Kauppinen P, Malmivuo J (2008) The influence of CSF on EEG sensitivity distributions of multi-layered head models. *IEEE Trans Biomed Eng* 55(4):1454–1456. <https://doi.org/10.1109/TBME.2007.912427>
- Wolters CH, Anwander A, Tricoche X, Weinstein D, Koch MA, MacLeod RS (2006) Influence of tissue conductivity anisotropy on EEG/MEG field and return current computation in a realistic head model: a simulation and visualization study using high-resolution finite element modeling. *Neuroimage* 30(3):813–826. <https://doi.org/10.1016/j.neuroimage.2005.10.014>
- Zaehle T, Clapp WC, Hamm C, Meyer D, Kirke J (2007) Induction of LTP-like changes in human auditory cortex by rapid auditory stimulation: an fMRI study. *Restor Neurol Neurosci* 25:251–259

Publisher's Note Springer Nature remains neutral with regard to jurisdictional claims in published maps and institutional affiliations.